Lanthanide-grafted hollow bipyridine-based Periodic Mesoporous Organosilicas as chemical sensors

Wanlu Liu [a b c], *Chunhui Liu* [b c], *Luca Pilia,*[d] *Hongliang Zhang,*[e] *Pascal Van Der Voort* [c], *Anna M. Kaczmarek* [b], *Rik Van Deun** [a]

a L^3 – Luminescent Lanthanide Lab, Department of Chemistry, Ghent University, Krijgslaan 281-S3, 9000 Ghent, Belgium.

b NanoSensing Group, Department of Chemistry, Ghent University, Krijgslaan 281-S3, 9000 Ghent, Belgium.

c Center for Ordered Materials, Organometallics and Catalysis (COMOC), Department of Chemistry, Ghent University, Krijgslaan 281-S3, 9000 Ghent, Belgium.

d *Department of Mechanical, Chemical and Materials Engineering, University of Cagliari, Via Marengo 2, 09123 Cagliari, Italy.*

e *Shenzhen University General Hospital, Shenzhen University, Shenzhen 518060, P.R. China.*

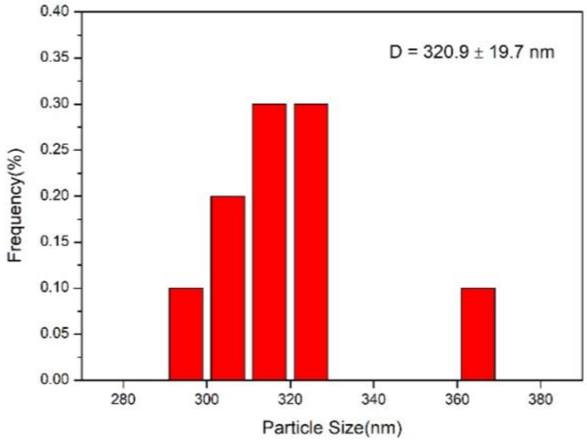

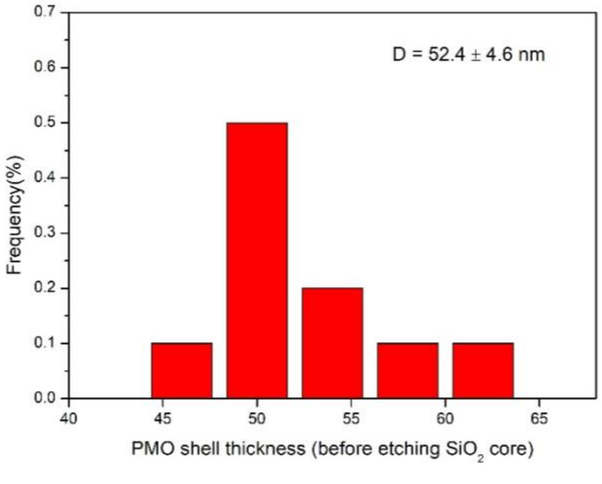

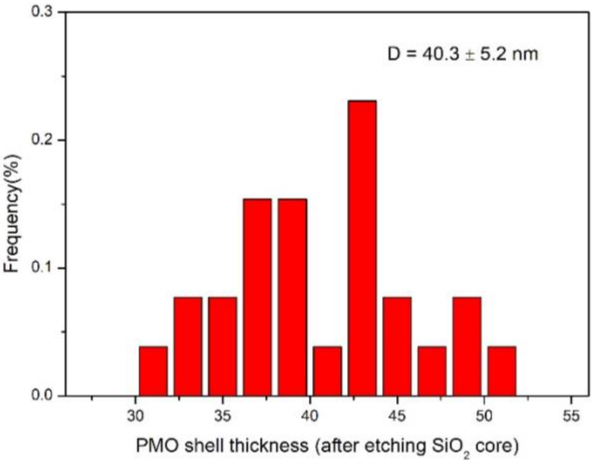

Figure S1. Top: particle size distribution diagram of Et-bpy-PMO@SiO_2; the PMO shell thickness distribution diagrams before (middle) and after etching SiO_2 core (bottom).

Table S1. Physicochemical properties of the PMOs studied in this research.

Sample	**S_{BET} (m^2/g)**	**V_p(cm^3/g)**	**D_p(nm)**
HEt-bpy-PMO	848	0.51	2.48
HEt-bpy-PMO@$EuCl_3$	711	0.46	2.40
HEt-bpy-PMO@$TbCl_3$	787	0.47	2.41
HEt-bpy-PMO@Eu_phen	630	0.38	2.44
HEt-bpy-PMO@Tb_phen	604	0.36	2.40
HEt-bpy-PMO@$Eu(tfac)_3$	711	0.43	2.43
HEt-bpy-PMO@$Tb(tfac)_3$	735	0.41	2.22

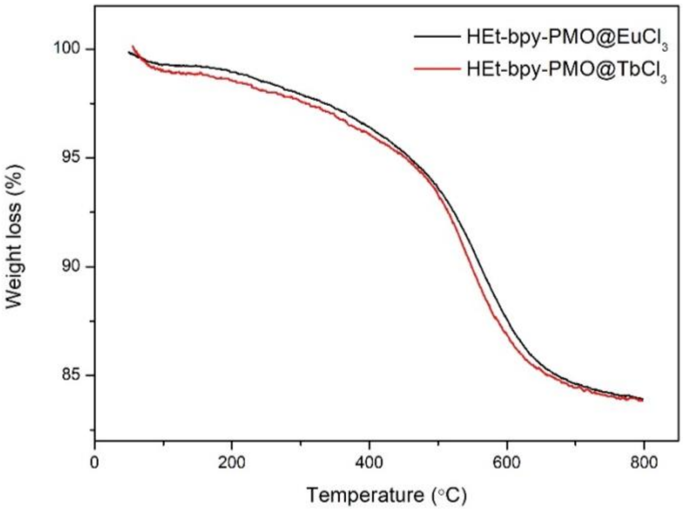

Figure S2. Thermogravimetric analysis (TGA) curves of HEt-bpy-PMO@$LnCl_3$(Ln = Eu, Tb).

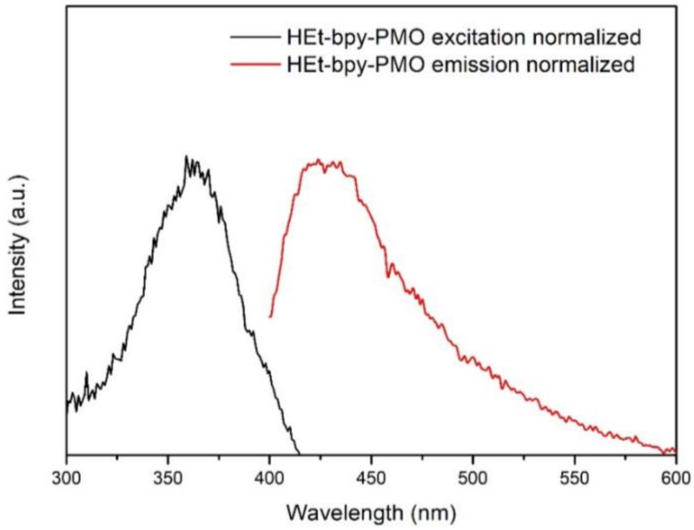

Figure S3. Left: excitation spectrum of HEt-bpy-PMO (monitored at 430 nm). Right: emission spectrum of HEt-bpy-PMO (excited at 365 nm).

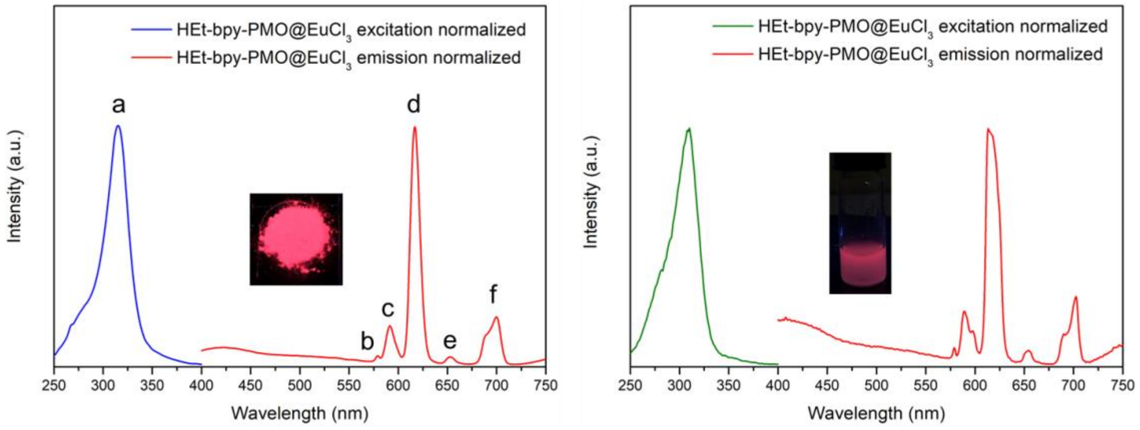

Figure S4. Left: solid-state combined excitation-emission spectrum of HEt-bpy-PMO@$EuCl_3$, right: combined excitation-emission spectrum of HEt-bpy-PMO@$EuCl_3$ in water suspension (1 mg/1 mL). Inset: photo taken when placing the sample under the UV lamp at an excitation wavelength of 302 nm. The emission spectra were recorded when exciting into the maximum of the broad ligand band and the excitation spectra were monitored at the $^5D_0 \rightarrow {}^7F_2$ transition peak.

Table S2. Assignment of peaks labeled in Figure S4 (HEt-bpy-PMO@$EuCl_3$ in solid-state).

Label	Wavelength (nm)	Transitions
	Excitation	
a	315	$\pi^* \leftarrow \pi$
	Emission	
b	579	$^5D_0 \rightarrow {}^7F_0$
c	591	$^5D_0 \rightarrow {}^7F_1$
d	617	$^5D_0 \rightarrow {}^7F_2$
e	653	$^5D_0 \rightarrow {}^7F_3$
f	700	$^5D_0 \rightarrow {}^7F_4$

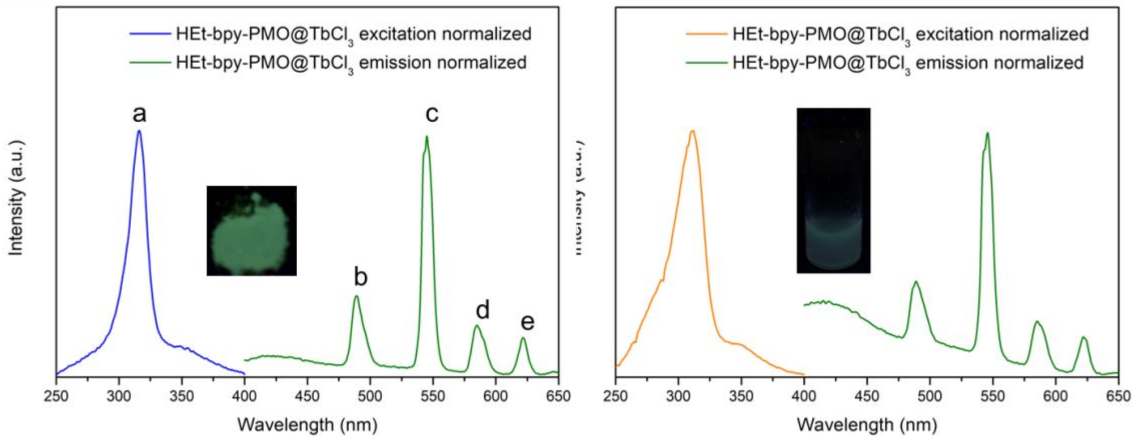

Figure S5. Left: solid-state combined excitation-emission spectrum of HEt-bpy-PMO@$TbCl_3$, right: combined excitation-emission spectrum of HEt-bpy-PMO@$TbCl_3$ in water suspension (1 mg/1 mL). Inset: photo taken when placing the sample under the UV lamp at an excitation wavelength of 302 nm. The emission spectra were recorded when exciting into the maximum of the broad ligand band and the excitation spectra were monitored at the $^5D_4 \rightarrow {}^7F_5$ transition peak.

Table S3. Assignment of peaks labeled in Figure S5 (HEt-bpy-PMO@$TbCl_3$ in solid-state).

Label	Wavelength (nm)	Transitions
	Excitation	
a	316	$\pi^* \leftarrow \pi$
	Emission	
b	489	$^5D_4 \rightarrow {}^7F_6$
c	545	$^5D_4 \rightarrow {}^7F_5$
d	585	$^5D_4 \rightarrow {}^7F_4$
e	621	$^5D_4 \rightarrow {}^7F_3$

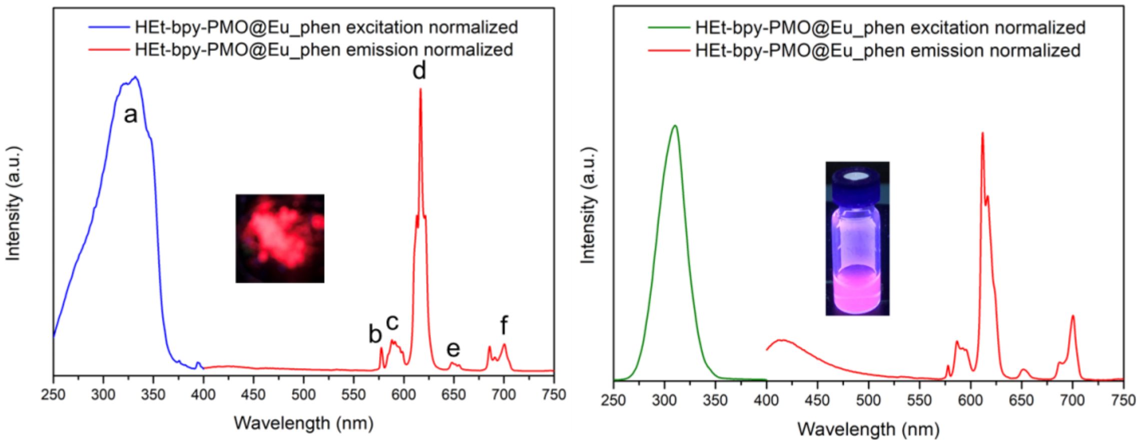

Figure S6. Left: solid-state combined excitation-emission spectrum of HEt-bpy-PMO@Eu_phen, right: combined excitation-emission spectrum of HEt-bpy-PMO@Eu_phen in water suspension (1 mg/1 mL). Inset: photo taken when placing the sample under the UV lamp at an excitation wavelength of 302 nm. The emission spectra were recorded when exciting into the maximum of the broad ligand band and the excitation spectra were monitored at the $^5D_0 \rightarrow {}^7F_2$ transition peak.

Table S4. Assignment of peaks labeled in Figure S6 (HEt-bpy-PMO@Eu_phen in solid-state).

Label	Wavelength (nm)	Transitions
	Excitation	
a	332	$\pi^* \leftarrow \pi$
	Emission	
b	577	$^5D_0 \rightarrow {}^7F_0$
c	591	$^5D_0 \rightarrow {}^7F_1$
d	617	$^5D_0 \rightarrow {}^7F_2$
e	650	$^5D_0 \rightarrow {}^7F_3$
f	700	$^5D_0 \rightarrow {}^7F_4$

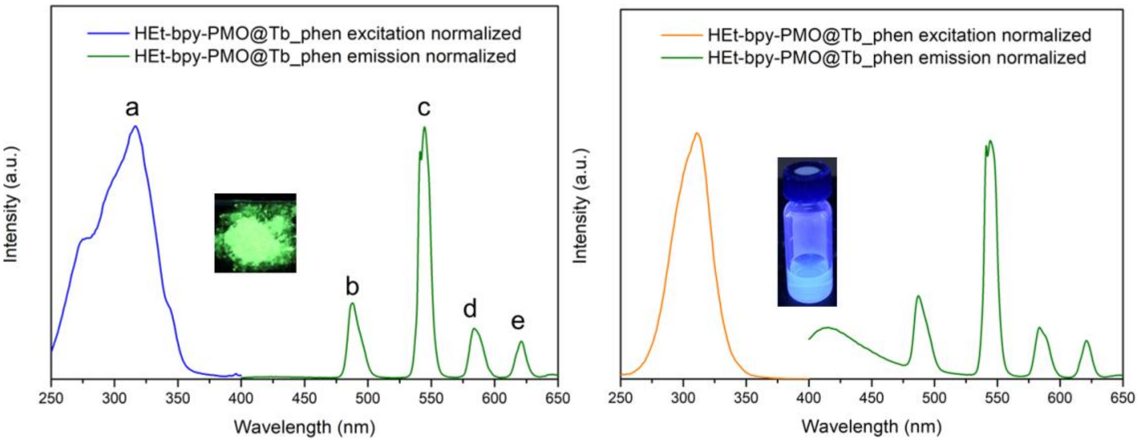

Figure S7. Left: solid-state combined excitation-emission spectrum of HEt-bpy-PMO@Tb_phen, right: combined excitation-emission spectrum of HEt-bpy-PMO@Tb_phen in water suspension (1 mg/1 mL). Inset: photo taken when placing the sample under the UV lamp at an excitation wavelength of 302 nm. The emission spectra were recorded when exciting into the maximum of the broad ligand band and the excitation spectra were monitored at the $^5D_4 \rightarrow {}^7F_5$ transition peak.

Table S5. Assignment of peaks labeled in Figure S7 (HEt-bpy-PMO@Tb_phen in solid-state).

Label	Wavelength (nm)	Transitions
	Excitation	
a	316	$\pi^* \leftarrow \pi$
	Emission	
b	489	$^5D_4 \rightarrow {}^7F_6$
c	545	$^5D_4 \rightarrow {}^7F_5$
d	585	$^5D_4 \rightarrow {}^7F_4$
e	621	$^5D_4 \rightarrow {}^7F_3$

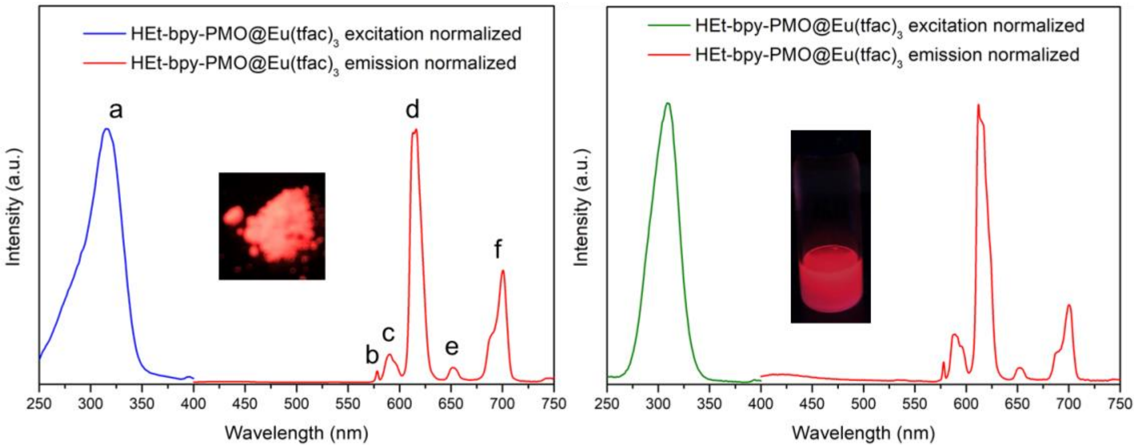

Figure S8. Left: solid-state combined excitation-emission spectrum of HEt-bpy-PMO@Eu(tfac)$_3$, right: combined excitation-emission spectrum of HEt-bpy-PMO@Eu(tfac)$_3$ in water suspension (1 mg/1 mL). Inset: photo taken when placing the sample under the UV lamp at an excitation wavelength of 302 nm. The emission spectra were recorded when exciting into the maximum of the broad ligand band and the excitation spectra were monitored at the $^5D_0\rightarrow{}^7F_2$ transition peak.

Table S6. Assignment of peaks labeled in Figure S8 (HEt-bpy-PMO@Eu(tfac)$_3$ in solid-state).

Label	Wavelength (nm)	Transitions
	Excitation	
a	315	$\pi^*\leftarrow\pi$
	Emission	
b	579	$^5D_0\rightarrow{}^7F_0$
c	591	$^5D_0\rightarrow{}^7F_1$
d	617	$^5D_0\rightarrow{}^7F_2$
e	652	$^5D_0\rightarrow{}^7F_3$
f	700	$^5D_0\rightarrow{}^7F_4$

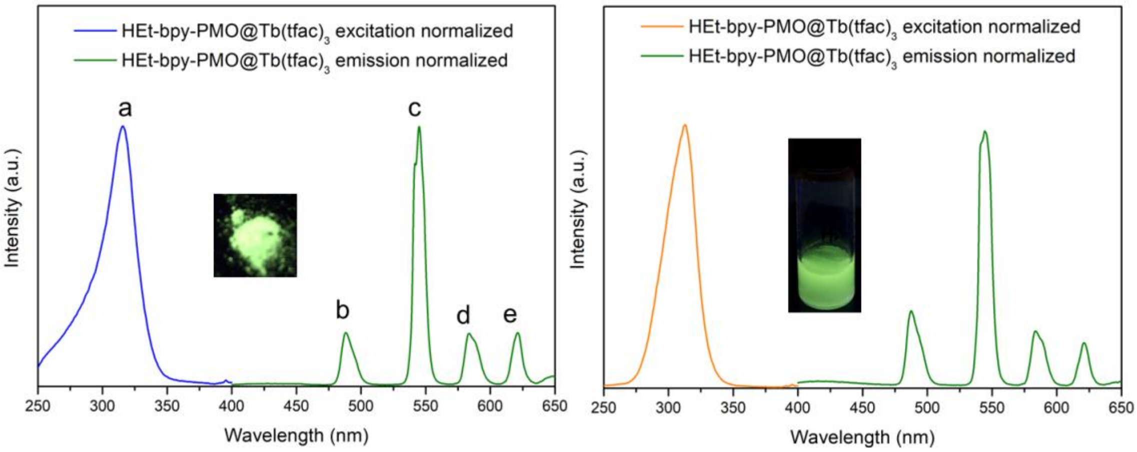

Figure S9. Left: solid-state combined excitation-emission spectrum of HEt-bpy-PMO@Tb(tfac)$_3$, right: combined excitation-emission spectrum of HEt-bpy-PMO@Tb(tfac)$_3$ in water suspension (1 mg/1 mL). Inset: photo taken when placing the sample under the UV lamp at an excitation wavelength of 302 nm. The emission spectra were recorded when exciting into the maximum of the broad ligand band and the excitation spectra were monitored at the $^5D_4\rightarrow{}^7F_5$ transition peak.

Table S7. Assignment of peaks labeled in Figure S9 (HEt-bpy-PMO@Tb(tfac)$_3$ in solid-state).

Label	Wavelength (nm)	Transitions
	Excitation	
a	316	$\pi^* \leftarrow \pi$
	Emission	
b	489	$^5D_4 \rightarrow {}^7F_6$
c	545	$^5D_4 \rightarrow {}^7F_5$
d	585	$^5D_4 \rightarrow {}^7F_4$
e	621	$^5D_4 \rightarrow {}^7F_3$

Table S8 The maximum of the ligand band of studied materials in the excitation spectra.

Sample	Wavelength (nm)	
	solid state	colloidal suspension
HEt-bpy-PMO@EuCl$_3$	315	310
HEt-bpy-PMO@TbCl$_3$	316	312
HEt-bpy-PMO@Eu_phen	332	310
HEt-bpy-PMO@Tb_phen	316	310
HEt-bpy-PMO@Eu(tfac)$_3$	315	309
HEt-bpy-PMO@Tb(tfac)$_3$	316	313

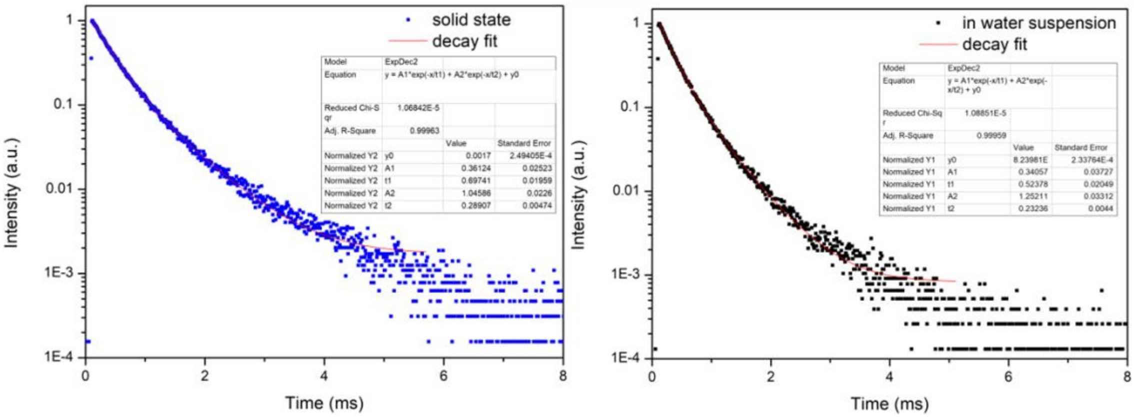

Model	ExpDec2		
Equation	y = A1*exp(-x/t1) + A2*exp(-x/t2) + y0		
Reduced Chi-Sqr	1.06842E-5		
Adj. R-Square	0.99963		
		Value	Standard Error
Normalized Y2	y0	0.0017	2.49405E-4
Normalized Y2	A1	0.36124	0.02523
Normalized Y2	t1	0.69741	0.01959
Normalized Y2	A2	1.04586	0.0226
Normalized Y2	t2	0.28907	0.00474

Model	ExpDec2		
Equation	y = A1*exp(-x/t1) + A2*exp(-x/t2) + y0		
Reduced Chi-Sqr	1.08851E-5		
Adj. R-Square	0.99959		
		Value	Standard Error
Normalized Y1	y0	8.23981E	2.33764E-4
Normalized Y1	A1	0.34057	0.03727
Normalized Y1	t1	0.52378	0.02049
Normalized Y1	A2	1.25211	0.03312
Normalized Y1	t2	0.23236	0.0044

Figure S10. Left: decay profile of HEt-bpy-PMO@EuCl$_3$ sample in solid-state form, right: decay profile of HEt-bpy-PMO@EuCl$_3$ sample in suspension. The decay times were recorded when exciting into the maximum of the broad ligand band and monitoring at the $^5D_0 \rightarrow {}^7F_2$ transition peak.

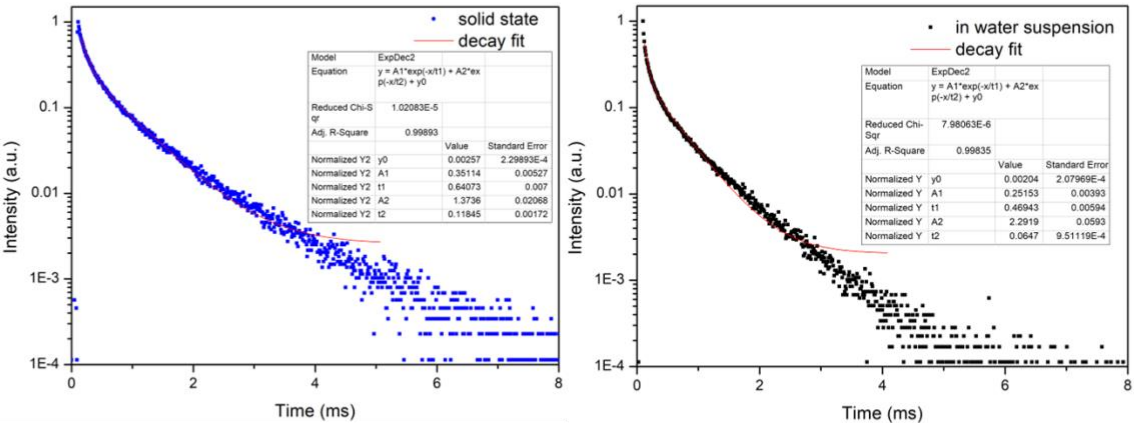

Model	ExpDec2		
Equation	y = A1*exp(-x/t1) + A2*exp(-x/t2) + y0		
Reduced Chi-Sqr	1.02083E-5		
Adj. R-Square	0.99893		
		Value	Standard Error
Normalized Y2	y0	0.00257	2.29893E-4
Normalized Y2	A1	0.35114	0.00527
Normalized Y2	t1	0.64073	0.007
Normalized Y2	A2	1.3736	0.02068
Normalized Y2	t2	0.11845	0.00172

Model	ExpDec2		
Equation	y = A1*exp(-x/t1) + A2*exp(-x/t2) + y0		
Reduced Chi-Sqr	7.98063E-6		
Adj. R-Square	0.99835		
		Value	Standard Error
Normalized Y	y0	0.00204	2.07969E-4
Normalized Y	A1	0.25153	0.00393
Normalized Y	t1	0.46943	0.00594
Normalized Y	A2	2.2919	0.0593
Normalized Y	t2	0.0647	9.51119E-4

Figure S11. Left: decay profile of HEt-bpy-PMO@TbCl$_3$ sample in solid-state form, right: decay profile of HEt-bpy-PMO@TbCl$_3$ sample in suspension. The decay times were recorded when exciting into the maximum of the broad ligand band and monitoring at the $^5D_4 \rightarrow ^7F_5$ transition peak.

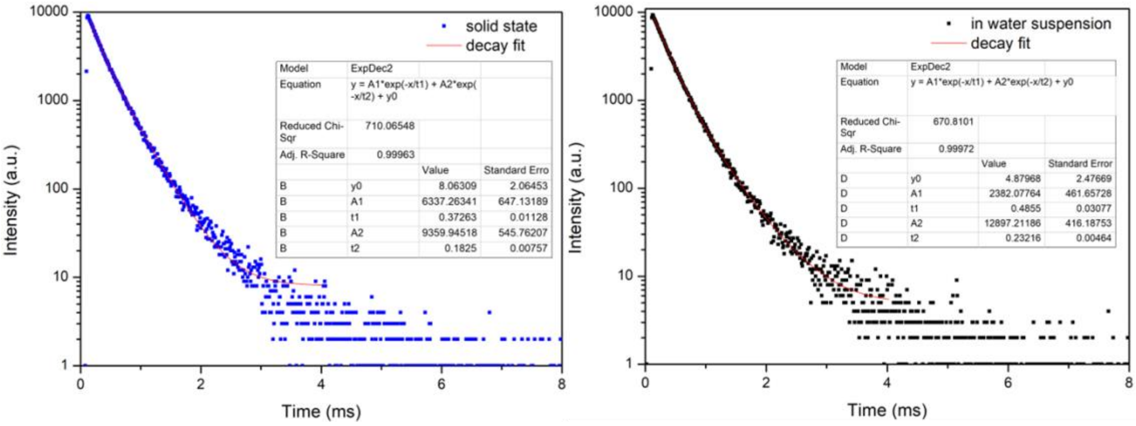

Model	ExpDec2		
Equation	y = A1*exp(-x/t1) + A2*exp(-x/t2) + y0		
Reduced Chi-Sqr	710.06548		
Adj. R-Square	0.99963		
		Value	Standard Erro
B	y0	8.06309	2.06453
B	A1	6337.26341	647.13189
B	t1	0.37263	0.01128
B	A2	9359.94518	545.76207
B	t2	0.1825	0.00757

Model	ExpDec2		
Equation	y = A1*exp(-x/t1) + A2*exp(-x/t2) + y0		
Reduced Chi-Sqr	670.8101		
Adj. R-Square	0.99972		
		Value	Standard Error
D	y0	4.87968	2.47669
D	A1	2382.07764	461.65728
D	t1	0.4855	0.03077
D	A2	12897.21186	416.18753
D	t2	0.23216	0.00464

Figure S12. Left: decay profile of HEt-bpy-PMO@Eu_phen sample in solid-state form, right: decay profile of HEt-bpy-PMO@Eu_phen sample in suspension. The decay times were recorded when exciting into the maximum of the broad ligand band and monitoring at the $^5D_0 \rightarrow ^7F_2$ transition peak.

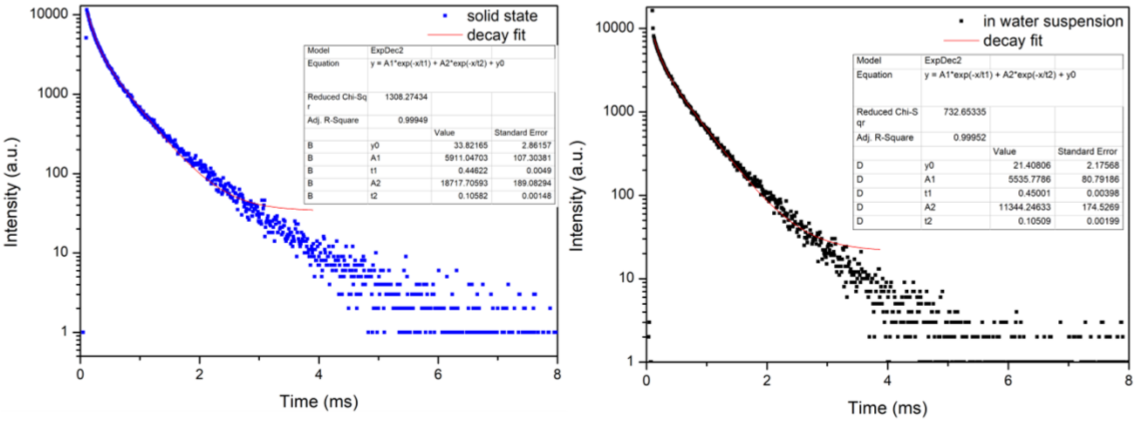

Model	ExpDec2		
Equation	y = A1*exp(-x/t1) + A2*exp(-x/t2) + y0		
Reduced Chi-Sqr	1308.27434		
Adj. R-Square	0.99949		
		Value	Standard Error
B	y0	33.82165	2.86157
B	A1	5911.04703	107.30381
B	t1	0.44622	0.0049
B	A2	18717.70593	189.08294
B	t2	0.10582	0.00148

Model	ExpDec2		
Equation	y = A1*exp(-x/t1) + A2*exp(-x/t2) + y0		
Reduced Chi-Sqr	732.65335		
Adj. R-Square	0.99952		
		Value	Standard Error
D	y0	21.40806	2.17568
D	A1	5535.7786	80.79186
D	t1	0.45001	0.00398
D	A2	11344.24633	174.5269
D	t2	0.10509	0.00199

Figure S13. Left: decay profile of HEt-bpy-PMO@Tb_phen sample in solid-state form, right: decay profile of HEt-bpy-PMO@Tb_phen sample in suspension. The decay times were recorded when exciting into the maximum of the broad ligand band and monitoring at the $^5D_4 \rightarrow ^7F_5$ transition peak.

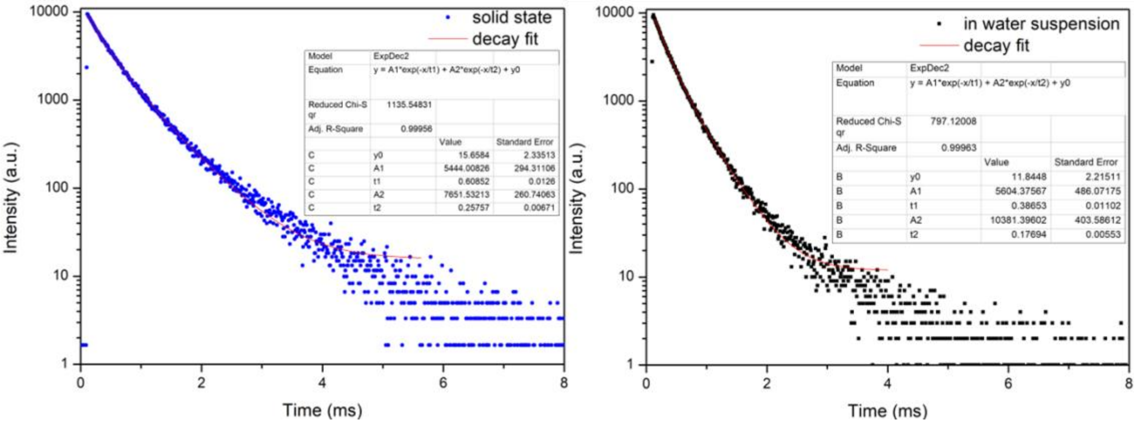

Model	ExpDec2		
Equation	y = A1*exp(-x/t1) + A2*exp(-x/t2) + y0		
Reduced Chi-Sqr	1135.54831		
Adj. R-Square	0.99956		
		Value	Standard Error
C	y0	15.6584	2.33513
C	A1	5444.00826	294.31106
C	t1	0.60852	0.0126
C	A2	7651.53213	260.74063
C	t2	0.25757	0.00671

Model	ExpDec2		
Equation	y = A1*exp(-x/t1) + A2*exp(-x/t2) + y0		
Reduced Chi-Sqr	797.12008		
Adj. R-Square	0.99963		
		Value	Standard Error
B	y0	11.8448	2.21511
B	A1	5604.37567	486.07175
B	t1	0.38653	0.01102
B	A2	10381.39602	403.58612
B	t2	0.17694	0.00553

Figure S14. Left: decay profile of HEt-bpy-PMO@Eu(tfac)$_3$ sample in solid-state form, right: decay profile of HEt-bpy-PMO@Eu(tfac)$_3$ sample in suspension. The decay times were recorded when exciting into the maximum of the broad ligand band and monitoring at the $^5D_0 \rightarrow {}^7F_2$ transition peak.

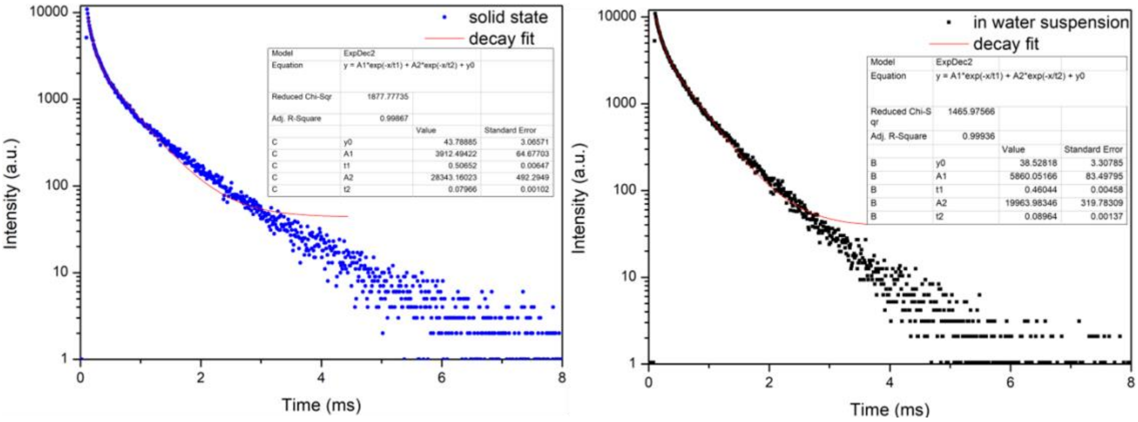

Model	ExpDec2		
Equation	y = A1*exp(-x/t1) + A2*exp(-x/t2) + y0		
Reduced Chi-Sqr	1877.77735		
Adj. R-Square	0.99867		
		Value	Standard Error
C	y0	43.78885	3.06571
C	A1	3912.49422	64.67703
C	t1	0.50652	0.00647
C	A2	28343.16023	492.2949
C	t2	0.07966	0.00102

Model	ExpDec2		
Equation	y = A1*exp(-x/t1) + A2*exp(-x/t2) + y0		
Reduced Chi-Sqr	1465.97566		
Adj. R-Square	0.99936		
		Value	Standard Error
B	y0	38.52818	3.30785
B	A1	5860.05166	83.49795
B	t1	0.46044	0.00458
B	A2	19963.98346	319.78309
B	t2	0.08964	0.00137

Figure S15. Left: decay profile of HEt-bpy-PMO@Tb(tfac)$_3$ sample in solid-state form, right: decay profile of HEt-bpy-PMO@Tb(tfac)$_3$ sample in suspension. The decay times were recorded when exciting into the maximum of the broad ligand band and monitoring at the $^5D_4 \rightarrow {}^7F_5$ transition peak.

Table S9 Luminescence decay times of studied materials ($\tau_{ave} = (A_1\tau_1^2+A_2\tau_2^2)/(A_1\tau_1+A_2\tau_2)$).

Sample	τ_1 (ms)	τ_2 (ms)	τ_{ave} (ms)
HEt-bpy-PMO@EuCl$_3$ solid	0.70	0.29	0.47
HEt-bpy-PMO@EuCl$_3$ suspension	0.52	0.23	0.34
HEt-bpy-PMO@TbCl$_3$ solid	0.67	0.12	0.42
HEt-bpy-PMO@TbCl$_3$ suspension	0.47	0.06	0.24
HEt-bpy-PMO@Eu_phen solid	0.37	0.18	0.29
HEt-bpy-PMO@Eu_phen suspension	0.49	0.23	0.30
HEt-bpy-PMO@Tb_phen solid	0.45	0.11	0.30
HEt-bpy-PMO@Tb_phen suspension	0.45	0.10	0.34
HEt-bpy-PMO@Eu(tfac)$_3$ solid	0.61	0.26	0.48
HEt-bpy-PMO@Eu(tfac)$_3$ suspension	0.39	0.18	0.29
HEt-bpy-PMO@Tb(tfac)$_3$ solid	0.51	0.08	0.31
HEt-bpy-PMO@Tb(tfac)$_3$ suspension	0.46	0.09	0.28

Table S10 Comparison between the proposed HEt-bpy-PMO@Eu(tfac)$_3$ and other reported porous materials for sensing of Co^{2+} and Cu^{2+}.

Porous material	Analyte	Detection solution	LOD (μM)	Ref.
ePMO@Eu_PA	Cu^{2+}	water	35.2	1
	Co^{2+}	water	26.9	
TH-PMO	Cu^{2+}	acetonitrile/water	0.04	2
BRhPMO	Cu^{2+}	ethanol/water	10	3
Tb-MOF	Co^{2+}	DMF	---	4
MOF-525	Cu^{2+}	DMF	0.067	5
Cd-MOF-74	Cu^{2+}	water	78.7	6
COF	Co^{2+}	water	0.00263	7
HEt-bpy-PMO@Eu(tfac)$_3$	Cu^{2+}	water	0.19	this work
	Co^{2+}	water	0.52	

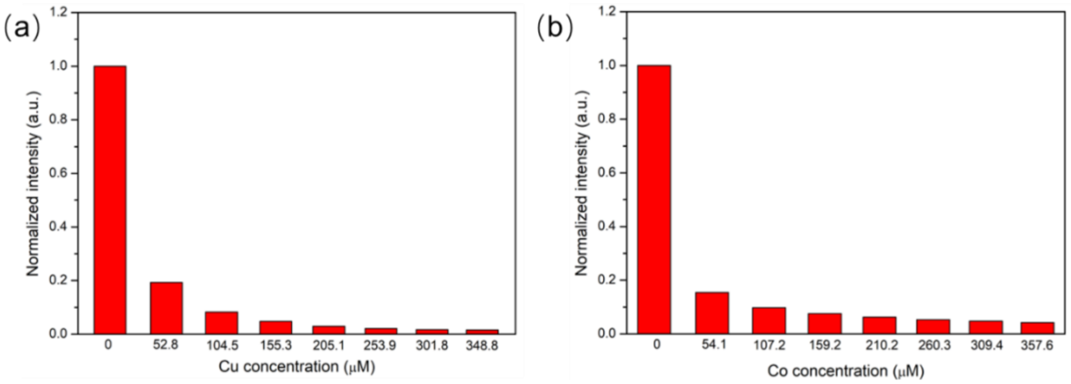

Figure S16. Normalized luminescence intensity of HEt-bpy-PMO@Eu(tfac)$_3$ suspension treated with different concentrations of (a) Cu^{2+} and (b) Co^{2+}.

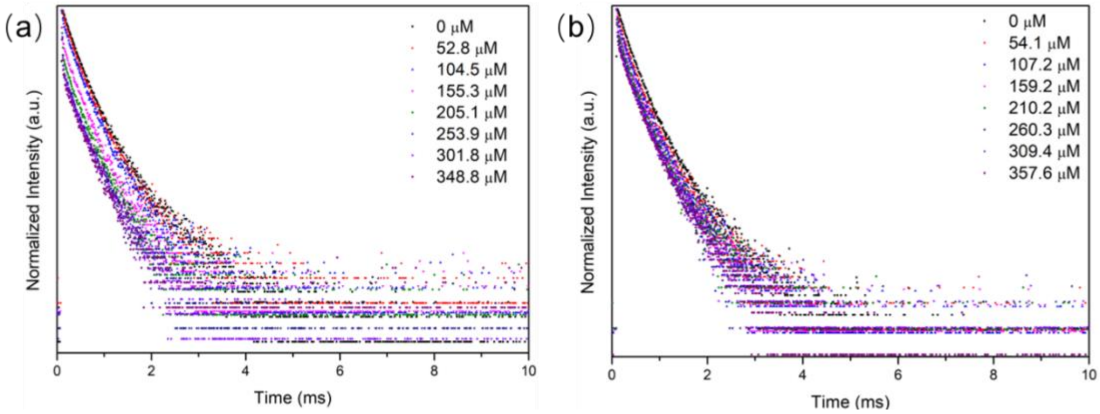

Figure S17. Luminescence decay times of an aqueous suspension of HEt-bpy-PMO@Eu(tfac)$_3$ observed at different concentrations of metal ions: (a) Cu^{2+} and (b) Co^{2+}.

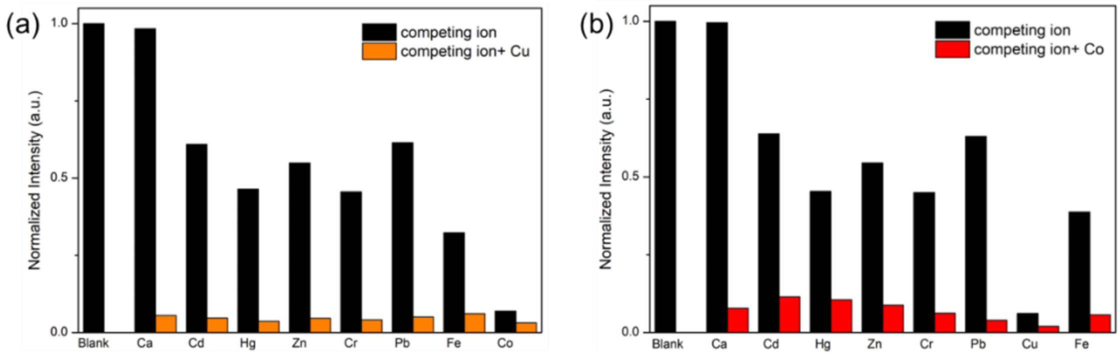

Figure S18. Luminescence emission intensity of HEt-bpy-PMO@Eu(tfac)$_3$ in the presence of a single competing ion (black bars) and in the mixture of competing ions and Cu^{2+} (a; orange bars) and Co^{2+} (b; red bars).

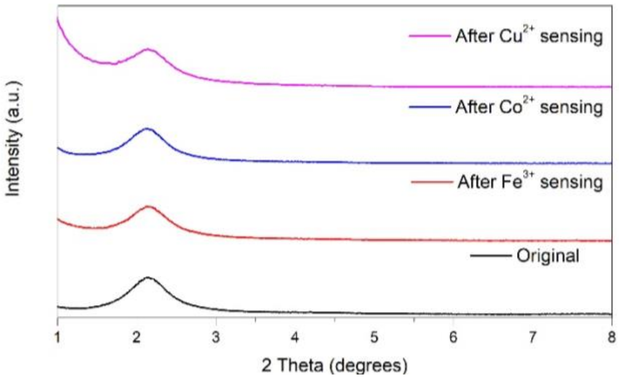

Figure S19. PXRD patterns of HEt-bpy-PMO@TbCl$_3$ after different treatment.

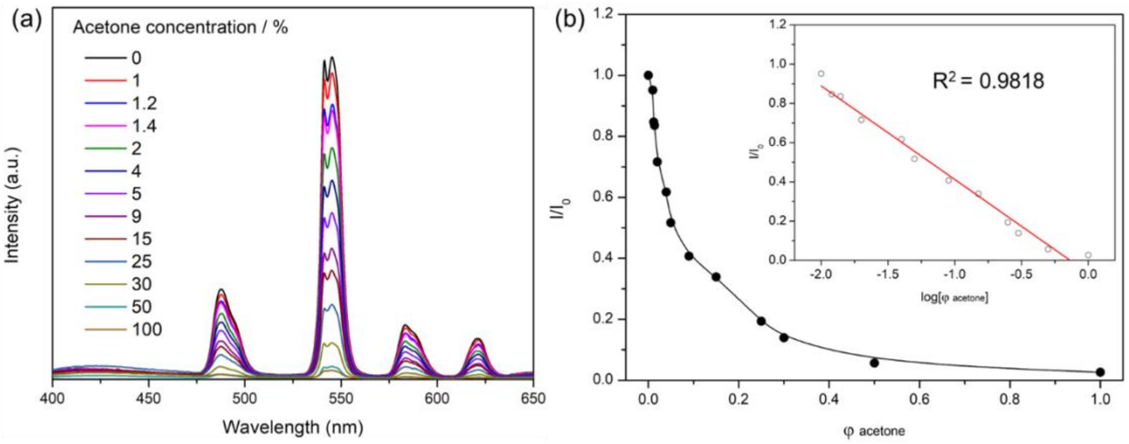

Figure S20. (a) Luminescence spectra of HEt-bpy-PMO@Tb(tfac)$_3$ as dispersions in mixed organic solvents (acetone / ethanol), (b) relationship between the I/I$_0$ and acetone volume (the inset is the relationship between the I/I$_0$ and the logarithm of acetone volume).

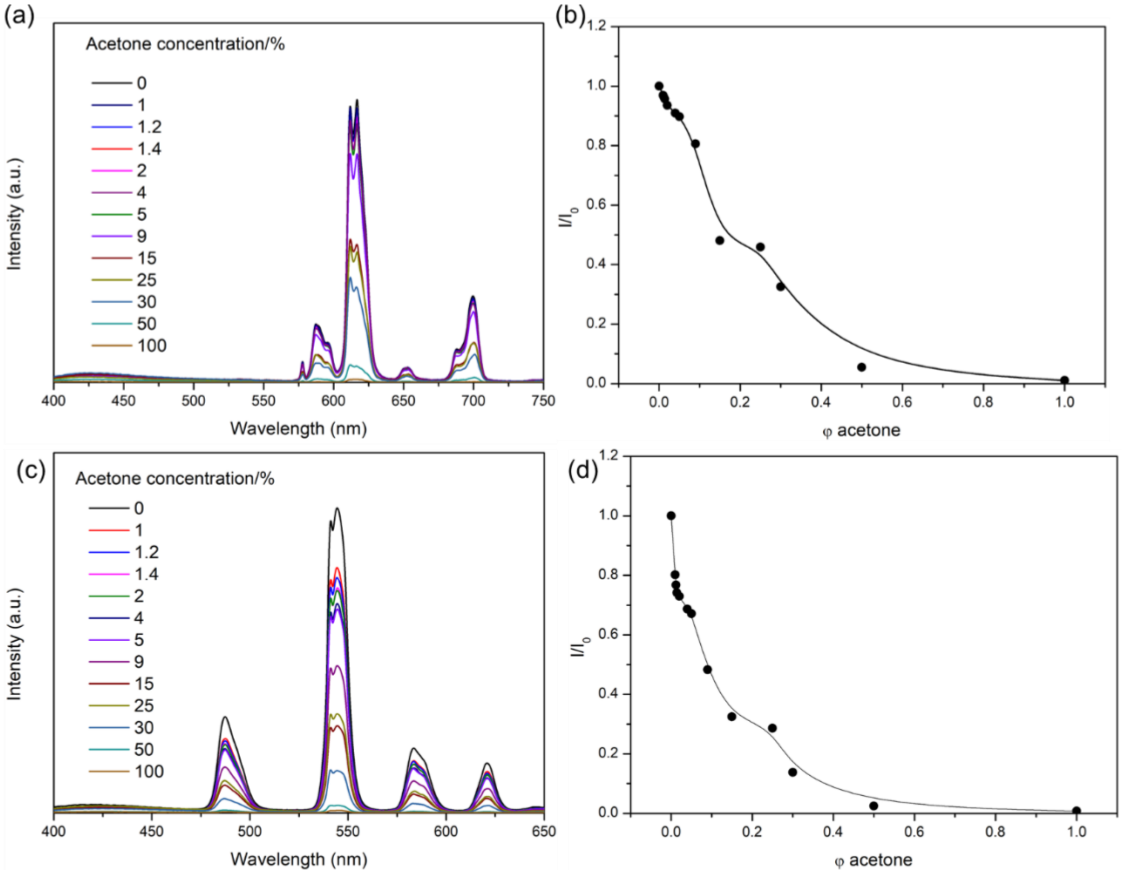

Figure S21. Luminescence spectra of (a) HEt-bpy-PMO@Eu(tfac)$_3$ and (c) HEt-bpy-PMO@Tb(tfac)$_3$ as dispersions in mixed acetone / water solvents. (b) and (d): relationship between the I/I$_0$ and acetone volume.

Table S11 Comparison between the proposed HEt-bpy-PMO@Ln(tfac)$_3$ (Ln = Eu, Tb) and other reported lanthanide porous materials for acetone sensing.

Porous material	LOD (vol %)	Ref.
DhaTab-COF-EuIL	1 %	8
$[Me_2NH_2]_2[(Eu)_2(ofdp)_2(DMF)(H_2O)]\cdot 7H_2O\cdot DMF$	7.4 %	9
$Eu(BTC)(H_2O)\cdot 1.5H_2O$	3.75 %	10
$Eu(FBPT)(H_2O)(DMF)$	5 %	11
$Yb(BPT)(H_2O)\cdot (DMF)_{1.5}\cdot (H_2O)$	5 %	12
$[Eu_4(BPT)_4(DMF)_2(H_2O)_8]$	5 %	13
HEt-bpy-PMO@Eu(tfac)$_3$	1 %	This work
HEt-bpy-PMO@Tb(tfac)$_3$	1 %	This work

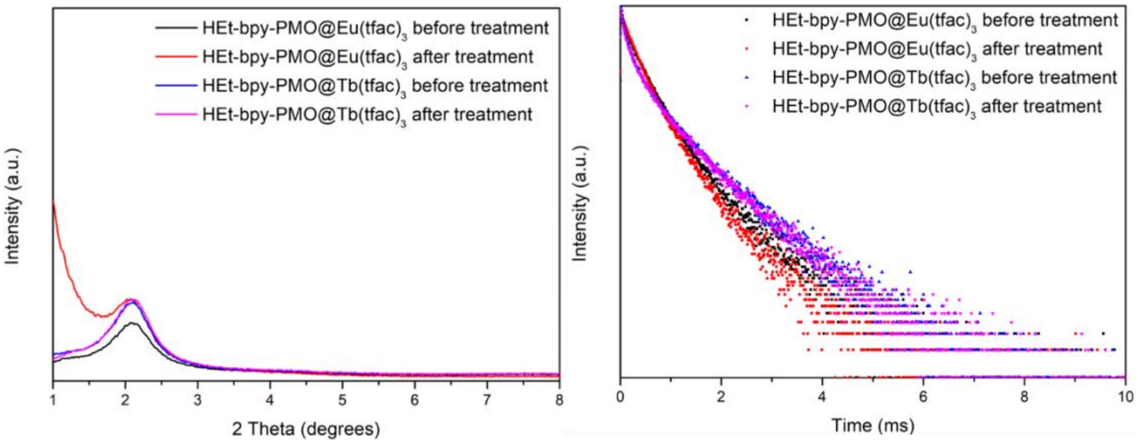

Figure S22. Powder XRD patterns (left) and decay profiles (right) of HEt-bpy-PMO@Eu(tfac)$_3$ and HEt-bpy-PMO@Tb(tfac)$_3$ before and after acetone sensing treatments.

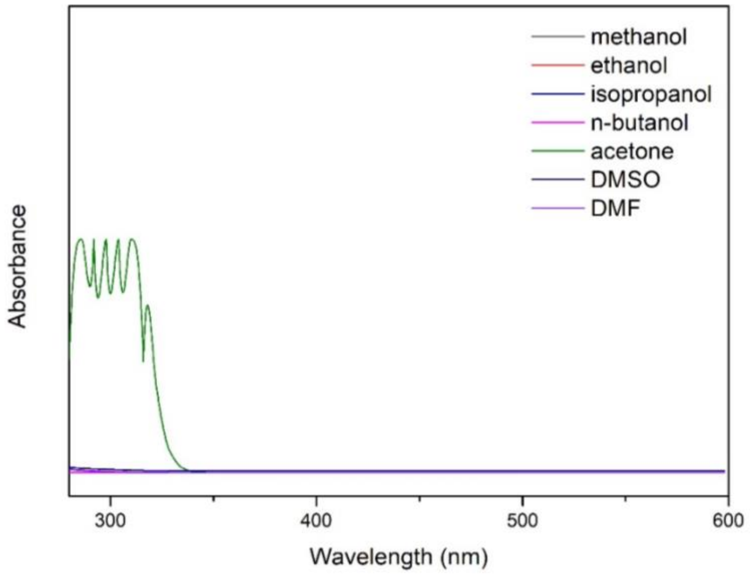

Figure S23. UV-vis spectra of methanol, ethanol, isopropanol, n-butanol, acetone, DMSO and DMF.

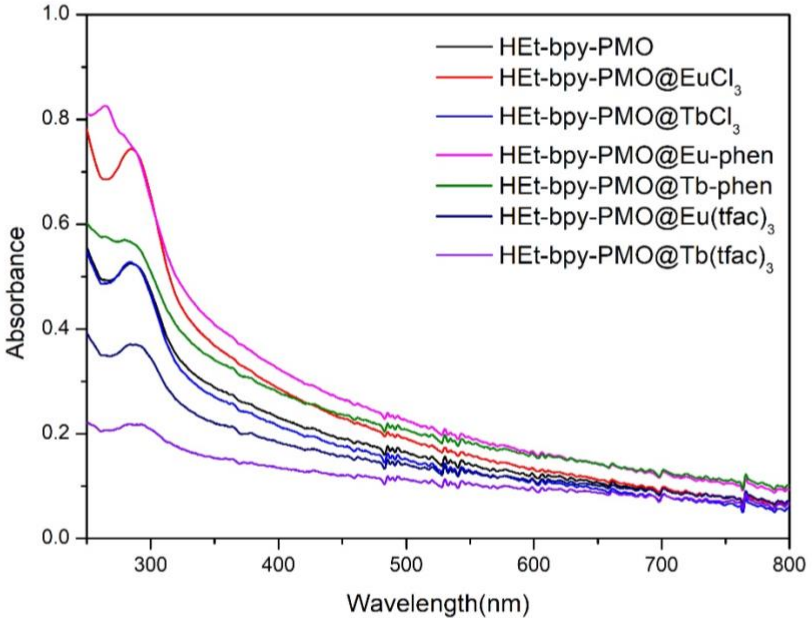

Figure S24. UV-vis spectra of HEt-bpy-PMO and HEt-bpy-PMO@Ln.

Given the importance of material stability in acidic and alkaline solutions for practical applications, HEt-bpy-PMO@Eu_phen was selected as an example to do further experiments. We recorded the luminescence spectra of HEt-bpy-PMO@Eu_phen in 11 solutions with different pH values (using the same measurement parameters).

The recyclability was examined by cyclic detection of pH at pH 4.83 and 10.11. After each treatment, the sample was centrifuged and washed with distilled water, and finally dried in an oven at 80 °C. The luminescence spectra of the recovered samples (in solid state) were measured to observe the luminescence intensity change (using the same measurement parameters).

Eventually, the final recovered sample was characterized by PXRD to evaluate the stability of HEt-bpy-PMO@Eu_phen.

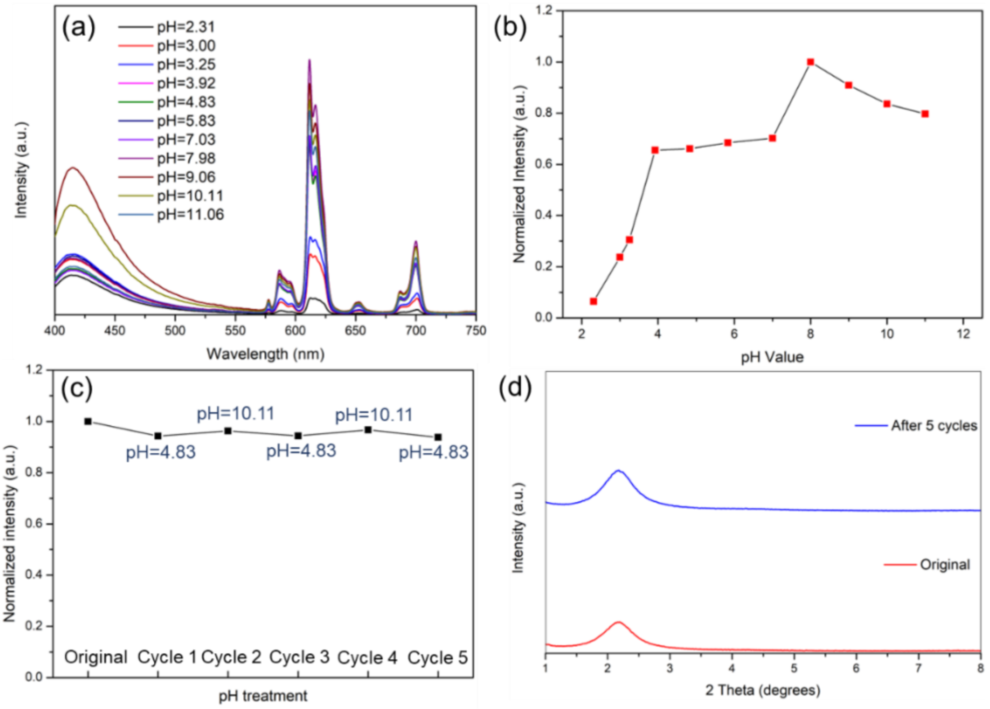

Figure S25. (a) pH dependent luminescence of HEt-bpy-PMO@Eu_phen in solutions with pH value ranging from 2.31 to 11.06. (b) normalized luminescence intensity I vs. pH plot. (c) normalized luminescence intensity I vs. cycle times after pH treatment. (d) PXRD patterns of HEt-bpy-PMO@Eu_phen before and after 5 cycles of pH sensing experiment.

DFT calculations

The ground-state electronic structure of 5,5'-Bis(triisopropoxysilyl)-2,2'-bipyridine ligand and acetone were calculated at Density Functional Theory (DFT)[14] level, employing the GAUSSIAN 16[15] software package, and using B3LYP[16,17] as functional and the valence triple-zeta 6-31+G(d,p)[18,19] as basis set. The ground state geometries were obtained in the gas phase by full geometry optimization without any symmetry constrain; furthermore, the absence of negative frequencies confirmed that the optimized geometries correspond to minima on the potential energy surfaces. All structures were input using *ArgusLab 4.0*.[20] The effects of solvation on the complexes were considered using the Polarizable Continuum Model (PCM); the ground state geometries were optimized in an acetone simulated electric field ($\varepsilon = 20.7$) starting from the gas phase optimized geometry.

References

1. W. Liu, A. M. Kaczmarek, H. Rijckaert, P. Van Der Voort and R. Van Deun, *Dalton Trans.*, 2021, **50**, 11061-11070.
2. M. Gao, S. Han, Y. Hu and L. Zhang, *J. Phys. Chem. C*, 2016, **120**, 9299-9307.
3. X. Qiu, S. Han, Y. Hu, M. Gao and H. Wang, *J. Mater. Chem. A*, 2014, **2**, 1493-1501.
4. Z. Cui, X. Zhang, S. Liu, L. Zhou, W. Li and J. Zhang, *Inorg. Chem.*, 2018, **57**, 11463-11473.
5. L. Li, S. Shen, R. Lin, Y. Bai and H. Liu, *Chem. Commun.*, 2017, **53**, 9986-9989.
6. T. T. Zheng, J. Zhao, Z. W. Fang, M. T. Li, C. Y. Sun, X. Li, X. L. Wang and Z. M. Su, *Dalton Trans.*, 2017, **46**, 2456-2461.
7. L. Wang, Y. Chen, Z. Zhang, Y. Chen, Q. Deng and S. Wang, *Mikrochim Acta*, 2021, **188**, 167.
8. H. Zuo, Y. Li and Y. Liao, *ACS Appl. Mater. Interfaces*, 2019, **11**, 39201-39208.
9. Y. Yang, L. Chen, F. Jiang, M. Wu, J. Pang, X. Wan and M. Hong, *CrystEngComm*, 2019, **21**, 321-328.
10. B. Chen, Y. Yang, F. Zapata, G. Lin, G. Qian and E. B. Lobkovsky, *Adv. Mater.* , 2007, **19**, 1693-1696.
11. Z. Hao, X. Song, M. Zhu, X. Meng, S. Zhao, S. Su, W. Yang, S. Song and H. Zhang, *J. Mater. Chem. A*, 2013, **1**, 11043-11050.
12. Z. Guo, H. Xu, S. Su, J. Cai, S. Dang, S. Xiang, G. Qian, H. Zhang, M. O'Keeffe and B. Chen, *Chem. Commun.*, 2011, **47**, 5551-5553.
13. Z. Hao, G. Yang, X. Song, M. Zhu, X. Meng, S. Zhao, S. Song and H. Zhang, *J. Mater. Chem. A*, 2014, **2**, 237-244.
14. R. G. Parr, W. Yang, Oxford University Press: Oxford, 1989.
15. Gaussian 16, Revision C.01, M. J. Frisch, G. W. Trucks, H. B. Schlegel, G. E. Scuseria, M. A. Robb, J. R. Cheeseman, G. Scalmani, V. Barone, G. A. Petersson, H. Nakatsuji, X. Li, M. Caricato, A. V. Marenich, J. Bloino, B. G. Janesko, R. Gomperts, B. Mennucci, H. P. Hratchian, J. V. Ortiz, A. F. Izmaylov, J. L. Sonnenberg, D. Williams-Young, F. Ding, F. Lipparini, F. Egidi, J. Goings, B. Peng, A. Petrone, T. Henderson, D. Ranasinghe, V. G. Zakrzewski, J. Gao, N. Rega, G. Zheng, W. Liang, M. Hada, M. Ehara, K. Toyota, R. Fukuda, J. Hasegawa, M. Ishida, T. Nakajima, Y. Honda, O. Kitao, H. Nakai, T. Vreven, K. Throssell, J. A. Montgomery, Jr., J. E. Peralta, F. Ogliaro, M. J. Bearpark, J. J. Heyd, E. N. Brothers, K. N. Kudin, V. N. Staroverov, T. A. Keith, R. Kobayashi, J. Normand, K. Raghavachari, A. P. Rendell, J. C. Burant, S. S. Iyengar, J. Tomasi, M. Cossi, J. M. Millam, M. Klene, C. Adamo, R. Cammi, J. W. Ochterski, R. L. Martin, K. Morokuma, O. Farkas, J. B. Foresman, and D. J. Fox, Gaussian, Inc., Wallingford CT, 2016.
16. D. Becke, *J. Chem. Phys.* 1993, **98**, 5648-5652.
17. C. Lee, W. Yang, R. G. Parr, *Phys. Rev. B* 1988, **37**, 785-789.
18. R. Krishnan, J. S. Binkley, R. Seeger, J. A. Pople, *J. Chem. Phys.* 1980, **72**, 650-654.
19. A. D. McLean, G. S. Chandler, *J. Chem. Phys.* 1980, **72**, 5639-5648.
20. M. A. Thompson, ArgusLab 4.0.1; Planaria Software LLC: Seattle, WA, http://www.arguslab.com/arguslab.com/ArgusLab.html/.